



UNIVERSITY OF LEEDS

This is a repository copy of *Crystallographic Structure, Intermolecular Packing Energetics, Crystal Morphology and Surface Chemistry of Salmeterol Xinafoate (Form I)*..

White Rose Research Online URL for this paper:

<https://eprints.whiterose.ac.uk/108859/>

Version: Accepted Version

---

**Article:**

Moldovan, AA [orcid.org/0000-0003-2776-3879](http://orcid.org/0000-0003-2776-3879), Rosbottom, I [orcid.org/0000-0001-6342-3973](http://orcid.org/0000-0001-6342-3973), Ramachandran, V et al. (3 more authors) (2017) Crystallographic Structure, Intermolecular Packing Energetics, Crystal Morphology and Surface Chemistry of Salmeterol Xinafoate (Form I). *Journal of Pharmaceutical Sciences*, 106 (3). pp. 882-891. ISSN 0022-3549

<https://doi.org/10.1016/j.xphs.2016.11.016>

---

© 2016 Elsevier. Licensed under the Creative Commons Attribution-NonCommercial-NoDerivatives 4.0 International <http://creativecommons.org/licenses/by-nc-nd/4.0/>

**Reuse**

Items deposited in White Rose Research Online are protected by copyright, with all rights reserved unless indicated otherwise. They may be downloaded and/or printed for private study, or other acts as permitted by national copyright laws. The publisher or other rights holders may allow further reproduction and re-use of the full text version. This is indicated by the licence information on the White Rose Research Online record for the item.

**Takedown**

If you consider content in White Rose Research Online to be in breach of UK law, please notify us by emailing [eprints@whiterose.ac.uk](mailto:eprints@whiterose.ac.uk) including the URL of the record and the reason for the withdrawal request.



[eprints@whiterose.ac.uk](mailto:eprints@whiterose.ac.uk)  
<https://eprints.whiterose.ac.uk/>

# Accepted Manuscript

Crystallographic Structure, Intermolecular Packing Energetics, Crystal Morphology and Surface Chemistry of Salmeterol Xinafoate (Form I)

Alexandru A. Moldovan, Ian Rosbottom, Vasuki Ramachandran, Christopher M. Pask, Oboroghene Olomukhoru, Kevin J. Roberts

PII: S0022-3549(16)41881-2

DOI: [10.1016/j.xphs.2016.11.016](https://doi.org/10.1016/j.xphs.2016.11.016)

Reference: XPHS 570

To appear in: *Journal of Pharmaceutical Sciences*

Received Date: 22 August 2016

Revised Date: 19 October 2016

Accepted Date: 11 November 2016

Please cite this article as: Moldovan AA, Rosbottom I, Ramachandran V, Pask CM, Olomukhoru O, Roberts KJ, Crystallographic Structure, Intermolecular Packing Energetics, Crystal Morphology and Surface Chemistry of Salmeterol Xinafoate (Form I), *Journal of Pharmaceutical Sciences* (2016), doi: 10.1016/j.xphs.2016.11.016.

This is a PDF file of an unedited manuscript that has been accepted for publication. As a service to our customers we are providing this early version of the manuscript. The manuscript will undergo copyediting, typesetting, and review of the resulting proof before it is published in its final form. Please note that during the production process errors may be discovered which could affect the content, and all legal disclaimers that apply to the journal pertain.



***Crystallographic Structure, Intermolecular Packing Energetics, Crystal Morphology and Surface Chemistry of Salmeterol Xinafoate (Form I)***

Alexandru A. Moldovan<sup>1</sup>, Ian Rosbottom<sup>1</sup>, Vasuki Ramachandran<sup>1</sup>, Christopher M. Pask<sup>2</sup>, Oboroghene Olomukhor<sup>1</sup>, Kevin J. Roberts<sup>1</sup>

<sup>1</sup>*Institute of Particle Science and Engineering and School of Chemical and Process Engineering, University of Leeds, Leeds, U.K.*

<sup>2</sup>*School of Chemistry, University of Leeds, Leeds, U.K.*

Communicating author: v.ramachandran@leeds.ac.uk

**Abstract**

Single crystals of salmeterol xinafoate (form I), prepared from slow cooled supersaturated propan-2-ol solutions, crystallise in a triclinic  $P\bar{1}$  symmetry with two closely related independent salt pairs within the asymmetric unit, with an approximately double unit cell volume compared to the previously published crystal structure<sup>1</sup>. Synthonic analysis of the bulk intermolecular packing confirms the similarity in packing energetics between the two salt pairs. The strongest synthons, as expected, are dominated by coulombic interactions. Morphological prediction reveals a plate-like morphology, dominated by the {001}, {010} and {100} surfaces, consistent with experimentally grown crystals. Though surface chemistry of the slow growing {001} face comprises of large sterically hindering phenyl groups, weaker coulombic interactions still prevail from the alcohol group present on the phenyl and hydroxymethyl groups. The surface chemistry of the faster growing {010} and {100} faces are dominated by the significantly stronger cation/anion interactions occurring between the carboxylate and protonated secondary ammonium ion groups. The importance of understanding the cohesive/adhesive nature of the crystal surfaces of an API, with respect to their interaction with other API crystals and excipients and how that may impact formulation design is highlighted.

**Keywords**

Molecular modelling, pulmonary drug delivery, crystal structure, polymorphism, morphology, synthonic engineering, salmeterol xinafoate, lattice energy, X-ray diffraction, formulation design, surface chemistry

**List of Symbols**

$E_{cr}$  = Lattice energy

$E_{att}$  = Attachment energy

$E_{sl}$  = Slice energy

$\epsilon_{hkl}$  = Surface specific anisotropy factor

kcal = kilocalories

**List of Terms**

DSC = Differential scanning calorimetry

SX = Salmeterol xinafoate

XRD = X-ray diffraction

vdW = van der Waals

H-bonds = Hydrogen bonds

API = Active Pharmaceutical Ingredient

**Introduction**

Salmeterol Xinafoate (2-(hydroxymethyl)-4-[1-hydroxy-2-[6-(4-(phenylbutoxy) hexylamino) ethyl] phenol, 1-hydroxynaphthalene-2-carboxylic acid (SX)) is a long-acting  $\beta_2$ -adrenoceptor agonist. It is commonly used on its own, or in combination with fluticasone propionate, for treating asthma. This material is present as the active pharmaceutical ingredient (API) in Serevent Diskus®, (GlaxoSmithKline).

SX is a salt that can exist in two crystalline polymorphic forms that exhibit an enantiotropic relationship, with form I being the stable polymorph and form-II being the metastable polymorph at ambient conditions<sup>2,3</sup>. Thermal studies of Salmeterol Xinafoate by *Beach et al.* observed that melting endotherms occurred at 122.7 °C and 137.6 °C, which were attributed to the melting of form I and form II respectively. Previous studies have suggested that the high contact temperatures induced by the milling process can produce seeds of form II, which are thought to then initiate the observed polymorphic transformation from form I to form II<sup>4-8</sup>. As a caveat to this, *Beach et al.* also showed that highly pure crystals of form I, prepared by solution enhanced dispersed supercritical fluids, did not show any significant evidence of polymorphic conversion, perhaps reflecting the absence of any form II seeds whilst using this process. This may suggest that the transformation kinetics between form I and form II are very slow. Although the crystallisation methods to obtain form I have been well described in the literature<sup>2,4,5,9,10</sup>, the challenges associated with the preparation and isolation of a required size single crystal for single crystal X-ray diffraction (XRD) have, so far, resulted in the crystal structure solution from powder XRD data<sup>1</sup>, the latter revealing apparent significant disorder around the phenyl group.

Servent Diskus© is marketed as an inhalation formulation, containing micronised drug particles that tend to form agglomerates with the carrier particles (excipients), and therefore must be effectively dispersed upon inhalation for optimum therapeutic value. To ensure effective dispersion, the balance between the cohesive (between homogeneous particles in the formulation) and adhesive (between heterogeneous particles in the formulation) forces is vital in the formulation design<sup>11,12</sup>.

Crystallographic and molecular modelling, utilising the atom-atom approach, has been extensively exploited to predict crystal morphologies<sup>13-20</sup> and identify the important bulk (intrinsic) and surface (extrinsic) intermolecular interactions (synthons), which can stabilise the crystal packing and influence face-specific crystal growth<sup>21-23</sup>. In formulation design, one or more excipients are selected for addition to the API. Excipients range from a lubricant to a bulking or a flavour enhancing agent. Excipients also play a major part in the stability and bioavailability of the drug and hence the key challenge is to choose the right excipient(s) for the API<sup>24-26</sup>. This can be achieved by identifying and classifying the API's extrinsic synthons. Knowledge of such interactions is helpful to assess API's binding to excipients (adhesive) or themselves (cohesive).

In the case of inhalation formulations, the micronised ingredients provide higher specific surface areas, resulting in increased van der Waals, electrostatic and capillary interactions. Hence they tend to form agglomerates thus exhibiting strong cohesion between homogeneous particles and adhesion between heterogeneous particles<sup>26,27</sup>. The balance of cohesion and adhesion will have an effect on the content uniformity in the formulation and the dispersibility in the lungs after inhalation. Therefore the understanding of the cohesive-adhesive balance is critical both in the formulation design as well as the product performance and bioavailability<sup>28,29</sup>. In a recent study, the cohesive-adhesive balance between the API and excipients of inhalation powders (fluticasone propionate, budesonide and salbutamol<sup>11,12</sup>) was investigated using molecular and crystallographic modelling tools. These simulations were successfully correlated to de-agglomeration data measured by laser diffraction<sup>30</sup> and highlights the applicability of this method to guide the formulation design of such inhalation powders, to achieve optimum efficacy. However, the application of these tools requires a crystal structure with well-resolved atom positions, along with an understanding of the bulk crystal and surface chemistry associated with the structure.

This paper reports the crystal structure of the form I of Salmeterol Xinafoate, as obtained using single crystal XRD data. Based on this, the intermolecular packing energetics, morphology and the surface chemistry of the morphologically important surfaces were characterised.

## Materials and Methods

### Materials

A supply of micronised SX was acquired from Vamsi Labs Ltd. (Chincholi, Solapur, Maharashtra, India) with batch number SX-0030513.

## Crystal Growth and Characterisation

### Single Crystal Growth

Salmeterol xinafoate single crystals were crystallised using a method based on a study presented by Murnane *et al.*<sup>4</sup>. A 1.6 w/v% suspension of SX was prepared. 10mg of SX was added to 0.625ml of propan-2-ol. This was then heated to 60 °C and stirred for 30 minutes. After maturing overnight at 45 °C it was then further cooled to 22 °C over 24 hours. The final suspension was filtered under vacuum and dried off in a desiccator for a further 24 hours. This method produced crystals of the size (50-250µm) and quality required to analyse by single crystal XRD.

### Optical Microscopy

An Olympus BX51, set in transmission mode utilising cross polarisation, with a UMPlanFl 10x/ 0.30 objective was utilised to analyse the size and shape of the crystals grown. The field and aperture diaphragms were adjusted to ensure optimum contrast and depth of field. QCaptureProV6.1. was used for measurements of the length and the width of the crystal.

### Differential Scanning Calorimetry (DSC)

The thermal profiles were produced using a Mettler Toledo DSC1. Approximately 1.5mg of the micronised and single crystal SX samples were weighed out into 40 µL alumina pans (Mettler Toledo). Samples were heated from 25 to 200 °C, with a rate of 2 °Cmin<sup>-1</sup>, and repeated to check for reproducibility.

### Single Crystal X-Ray Diffraction

A suitable single crystal was immersed in inert oil and mounted on a nylon loop. The crystal was then cooled to 120 K using an Oxford Cryosystems 700 Series Cryostream Cooler<sup>31</sup> and data collected on a RigakuSuperNova diffractometer fitted with an Atlas CCD detector with monochromated Mo-K $\alpha$  radiation ( $\lambda = 0.71073 \text{ \AA}$ ). The dataset was collected and processed using CrysAlisPRO<sup>32</sup> and corrected for absorption using an analytical numeric correction<sup>33</sup>; the structure solved using SHELXS<sup>34</sup> and refined by full-matrix least squares on F<sup>2</sup> using ShelXL-2014<sup>35</sup> interfaced through the programme Olex2<sup>36</sup>. Molecular graphics and tables of data were produced using Olex2<sup>36</sup>. All non-hydrogen atoms were located in the Fourier Map and refined anisotropically. All hydrogen atoms bound to carbon were placed in calculated positions and refined isotropically using a “riding model”.

### Computational Analysis

The computational analysis was carried out utilising Mercury<sup>37</sup>, HABIT98<sup>38</sup> and Accelrys software Materials Studio<sup>39</sup> (MS). Structural optimisation, through lattice energy minimisation, was performed in MS utilising the Forcite module, Dreiding forcefield<sup>40</sup> and Gasteiger charges<sup>41</sup>. The conformation was allowed to relax whilst maintaining periodicity, and the unit cell parameters were held rigid.

The strength and nature of the intermolecular synthons, the lattice energy ( $E_{cr}$ ) and hence the slice ( $E_{sl}$ ) and attachment ( $E_{att}$ ) energies, were calculated within HABIT98 using the potential parameters published by Momany *et al.*<sup>42</sup>, with the Evjen summation method<sup>43</sup> to ensure charge neutrality. The former is particularly appropriate for modelling organic crystals containing amide and carboxylic acid groups<sup>42</sup>. The programme creates a nest of unit cells in three dimensions and calculates all the interactions within a user-defined sphere. The lattice energy was calculated at sphere radii between 10-115 Å to test and ensure convergence of the lattice energy.

The intermolecular synthons contributing to the lattice energy was divided into slice and attachment energies, according to Equation 1.

$$E_{cr} = E_{sl} + E_{att} \text{ (Equation 1)}$$

The attachment energies were scaled as relative growth rates per surface and used to construct a Wulff plot<sup>44</sup> within Mercury to predict the crystal morphology.

The surface anisotropy factor ( $\epsilon_{hkl}$ ) was calculated to assess the degree of synthon broken upon surface termination of the bulk crystal chemistry, with respect to the resultant surface chemistry<sup>45,46</sup>, using Equation 2.

$$\epsilon_{hkl} = \frac{E_{hkl}^{sl}}{E_{cr}} \text{ (Equation 2)}$$

All anisotropy factors were given as a percentage.

The methodologies associated with the ranking of the intermolecular synthons and the lattice energy breakdown have been described in previous publications<sup>21,30</sup>. The contribution of the functional groups to the lattice energy was calculated by summing the individual constituent atom contributions to the lattice energy, calculated in HABIT98. All visualisation of molecular and crystal packing was carried out in Mercury and Materials Studio.

## Results and Discussion

### Crystal Growth and Characterisation

The solution grown crystals were formed with good optical quality and displayed a plate-like morphology, with sizes ranging from 57-200 $\mu\text{m}$  along the longest axis. One of the largest crystals is shown in Figure 1(a).

Figure 2 shows the DSC profiles of the as received micronised sample (plotted as dashed) and the re-crystallised sample (plotted as solid). The micronised sample revealed two endotherms, in good agreement with the previously published melting points for form I and form II<sup>2</sup>, along with an exotherm at  $\sim 128$  °C, which can be attributed a re-crystallisation event which is consistent with the polymorphic transformation from form I to form II<sup>2</sup>. In comparison, the re-crystallised sample showed a much lower peak intensity for the latter transformation, suggesting a much lower concentration of form II. This data is in good agreement with previous studies<sup>2</sup>.

Crystallographic data from the single crystal XRD has been tabulated in Table 1. Form I was found to crystallise in a centrosymmetric triclinic structure (space group  $P\bar{1}$ ) with a tetra-molecular unit cell ( $Z=2$ ,  $Z'=4$ ), with two crystallographically independent anion/cation pairs of salmeterol and xinafoate, labelled SA1, SA2, XI1 and XI2. Hydrogen atoms bound to heteroatoms (O, N) were located in the Fourier Map and refined isotropically, apart from O3A,B, which were placed in calculated positions. The packing of the unit cell is illustrated in Figure 3a, with the different colours referring to the symmetrically equivalent ions from the asymmetric unit. The packing of molecules in Figure 4 shows that the major H-bonds and anion-cation interactions are orientated closest to the a and b axes directions with less of these interactions being orientated close to the c-axis direction. An examination of the differences in the Fourier Map of the electron density revealed the presence of some disorder within the crystal structure, specifically the nature of disorder between two salmeterol molecules. SA1 exhibited residual electron density, consistent with the alcohol group being disordered between two positions, with both S (major) and R (minor) isomers being present. The occupancies of the oxygen atoms were refined to 90% and 10% (S and R respectively). C-O bond lengths were restrained to 1.430 (5) Å and O3B (minor component) was refined isotropically to ensure stable refinement. Blue circles on Figure 3b highlights the position of the disorder.

The SA2 molecule exhibited slightly more disorder on the  $(\text{CH}_2)_3(\text{C}_6\text{H}_5)$  groups across these two positions, with the occupancies of the two components being refined to 70% and 30% respectively. An enhanced rigid-bond restraint (RIGU)<sup>47</sup> was applied to the anisotropic displacement parameters of the minor disordered component to obtain more sensible parameters than could be obtained without using this technique. Blue circles on Figure 3c highlights the position of the disordered molecular groups on the salmeterol cations. Based on the disorder positions refined from the single crystal XRD, the dominant atomic positions (90% occupancy of the oxygen atom of the alcohol group of SA1 and 70% occupancy of the  $(\text{CH}_3)_2(\text{C}_6\text{H}_5)$  on SA2) were taken forward for the intermolecular energetics, morphology and surface chemistry calculations. Coordinates of the disordered functional group components have been tabulated in Supplementary Material.

### Conformational Analysis

The presence of the two salt pairs within the asymmetric unit was found to reflect the conformational difference of the salmeterol ions. Figure 5b highlights the differences between the two salmeterol ions, revealing that the main conformational change occurs due to rotation of the C-C bond that is adjacent to the ether group on SA2, of around  $\sim 107^\circ$ . This results in a significant difference in orientation for the phenyl ring between the two salmeterol ions (Figure 5a). As might be expected, there was no significant difference in conformation between the xinafoate ions.

### Comparison to Previous Structure

The cell parameters of form I are listed in Table 2 (Structure in CCDC, 1483119) and compared with the previously published powder XRD parameters<sup>1</sup>. The cell parameter along the b axis, which was 9.484 Å from the powder XRD<sup>1</sup>, was found to be extended to almost double that value, at 16.122 Å from the single crystal XRD structure. The previous structure<sup>1</sup> showed packing of crystallographically equivalent salmeterol and xinafoate ions along the b-axis. However, the identification of the two crystallographically independent salt pairs within the asymmetric unit effectively doubles the unit cell vector along the b-axis.

The previous structure<sup>1</sup> showed a disorder around the phenyl ring of the salmeterol ion, which was modelled, in that study, using a thermal ellipsoid to account for the uncertainty. A comparison of the packing arrangement of the two structures does though reveal the same network of hydrogen bonding interactions, indicating a broad consistency of the solid state structures.

### Key Intermolecular Synthons in Solid State

The lattice energy converged to -67.75 kcal/mol (Figure 6) at a greater limiting radius, when compared to previous studies of molecular crystals<sup>21,48</sup>. The latter probably reflects the fact that the coulombic interactions, between the charged species, are much longer range than van der Waals (vdW) or hydrogen bonding interactions (H-bonds). Figure 6 also shows that the coulombic interactions (red line) accounted for almost half of the lattice energy. Figure 7 shows diagrammatically how the constituent molecular fragments of the salt pair contribute to the calculated lattice energy. The summation of the atom and functional group contributions revealed that the COO<sup>-</sup> ( $\delta$ ) group had the greatest contribution to the calculated lattice energy, reflecting its intimate involvement with the strong coulombic anion-cation interactions. Groups  $\beta$  and  $\gamma$  were found to have similar contributions. However it is likely that group  $\beta$  will have more directional interactions due to the charged atoms within this group, along with the interactions being focussed onto significantly fewer atoms than group  $\gamma$ . Groups  $\alpha$  and  $\epsilon$ , which are dominated by the aromatic ring structures, were found to contribute less to the calculated lattice energy than the other groups. This perhaps reflects the fact that the packing considerations for large molecules, such as salmeterol, can preclude the close alignment of the aromatic groups and hence the kind of strong pi-pi stacking interactions that have been observed within the crystal structures of smaller aromatic molecules<sup>21,49,50</sup>, which can contribute more significantly to the lattice energy.

Table 3a shows the top twelve strongest attractive synthons found from the analysis of the bulk crystal structure. All of the most attractive synthons were found to be between the anion-cation pairs, reflecting the dominant interactions resulting from the coulombic forces. Also, due to the symmetrical inequivalency of the salt pairs, the synthon types were often found to be very similar to each other and simply occurring between the different symmetrically inequivalent ions. This is indicated in column 2 of Table 3, which identifies the ions that make up the synthon; along with Figure 8, which shows the molecular orientation of the strongest synthon types.

Figure 8 reveals that the orientation of the specific atoms strongly influences the strength of the synthon. Synthons A<sub>a</sub>/B<sub>a</sub> have the closest orientation of the oppositely charged COO<sup>-</sup> and NH<sub>2</sub><sup>+</sup>, resulting in a very strong coulombic interaction. This synthon contained a H-bonding network consisting of one intra and two intermolecular H-bonds, due to the close proximity of the donor H's on the NH<sub>2</sub><sup>+</sup> group and acceptor O's on the COO<sup>-</sup> group. The added attractive force of these H-bonds probably contributes to this synthon being calculated as the most attractive within the structure. However, the calculations indicated that the majority of the energy of this synthon is still produced by

the electrostatic interactions between the oppositely charged atoms. It was also observed that, in general, as the distance between the  $\text{COO}^-$  and  $\text{NH}_2^+$  groups increases, the attractive force between the ions decreases. However, even though the  $\text{COO}^-$  and the  $\text{NH}_2^+$  groups are closer in synthon  $L_a$ , synthons  $I_a/K_a$  and  $J_a$  were calculated to have a greater attractive interaction due to these synthons forming greater vdW and H-bonding interactions respectively.

Though the two ions have six H-bond donor atoms and eight H-bond acceptor atoms between them, the only other synthon to have a significant H-bond is  $J_a$ , where the  $\text{COO}^-$  group of the xinafoate ion is orientated close to the OH group which is directly on the phenyl ring of salmeterol. This indicates that the H-bonding probably doesn't influence the stability of this crystal structure as much when compared to how it can affect the stability of a small molecule molecular crystal<sup>21,51,52</sup>. The combination of the strong electrostatic interactions and the fact that salmeterol has relatively large molecular weight (603.745 g/mol), which gives it a greater capacity to form stronger vdW interactions, has probably resulted in the decreased influence of H-bonds on the stability and physical properties of this structure.

The strongest repulsions within the crystal structure were found to be between the anionic xinafoate ions, shown in Figure 9. Due to the symmetrical equivalence of the anions, the most repulsive four independent pairs are illustrated. Table 3b shows that, as expected, the majority of the repulsion energy is due to the coulombic repulsions. These repulsive synthons were found to be between 7.17 Å and 9.57 Å apart (carbonyl C-carbonyl C). These repulsions were more than compensated for by the strong attractive forces between the anion-cation pairs. Hence the crystal structure was found to be stable, even in the presence of these repulsions.

### Morphology and Surface Chemistry

Figure 1b shows that the predicted morphology compares well with the experimental data (Figure 1a). However the observed crystal has a greater aspect ratio than the predicted morphology. The cleaved {100}, {010} and {001} surfaces are shown in Figure 1b. The top three extrinsic synthons that are contributing to the attachment energies of each plane are tabulated in Table 4. The {001} surface was calculated to have an attachment energy of -4.51 kcal/mol, hence being predicted to be the slowest growing surface. The strongest bulk attractive synthons lay within the slice, and as such the terminal functional groups on the surface that would be expected to influence the growth are large sterically hindering phenyl from SA1 and alcohol group extended from the phenyl group from SA2. Table 4 reveals that the strongest synthon that contributes to the attachment energy of the {001} surface had an energy of -5.32 kcal/mol, which is much less than the energies of the strongest synthons that are shown in Table 3. These synthons were both found to be mainly dominated by the  $\text{COO}^- \cdots \text{NH}_2$  interactions as well as  $\text{COO}^- \cdots \text{OH}$  present on the phenyl ring.

In contrast, the {010} plane was predicted to be the fastest growing with an attachment energy of -24.78 kcal/mol, which was attributed to the position of the terminal anion, allowing for a much greater electrostatic attraction at the surface and thus growth in the given direction. Table 5 shows that synthon  $B_a$  has the highest contribution to the attachment energy of the {010} surface, at -29.94 kcal/mol. The dominant interaction within this synthon is based on the strong coulombic interactions between the salt pairs. Similarly, the synthons containing the strong coulombic interactions between the salt pairs were also predicted to contribute strongly to the attachment energy of the {100} surface. Hence this is also predicted to be much faster growing and smaller than the dominant {001} surface.

The % surface saturation (anisotropy factors) are shown in Table 4. As expected, the {001} surface contains the highest degree of saturation, 93.4%, due to less of the strong synthons being broken at the surface. In comparison the {010} and {100} surfaces which have 64.41% and 65.52% saturation respectively, as they are predicted to have strong anion/cation synthons broken at their respective surfaces. Due to the higher degree of unsaturation, it can be expected from a formulation design perspective, that the edges of the crystals will have cohesively higher binding affinity than for the larger more dominant facets. This has been observed in previous studies of the crystallisation behaviour of paracetamol crystals<sup>53-55</sup>, where the crystals appeared to agglomerate through the binding of the smaller side, rather than the large flat, stable surface. The latter might suggest why micronised APIs are often preferred in the practical formulation, since the majority of the natural surface of the as-grown single crystals of this compound



may be expected to show poor adhesivity and cohesivity to excipients and other API crystals respectively. The micronisation procedure can be expected to lower the surface energy of the crystal surfaces<sup>27,56-59</sup>, by exposing higher energy fracture planes, which can exhibit lower degrees of synthon saturation with much greater potential for surface bonding<sup>60</sup>, and as such, this probably improves the adhesive behaviour of the API.

## Conclusion

The re-crystallisation and characterisation of Salmeterol Xinafoate form I has been carried out revealing a crystal structure that contains two crystallographically independent salt pairs, associated with conformational differences between the two salmeterol ions. This provides an update and further refinement on the previous structure that predicted only one salt pair within the asymmetric unit. Synthonic modelling revealed the extent of the importance of coulombic interactions between the salt pairs to stabilise the lattice energy, and suggested that even though there are H-bonds within the crystal structure, their influence is much reduced in salt structures when compared to lower molecular weight crystal structures. The prediction of a crystal morphology containing three major faces was consistent with the general shape observed from solution grown crystals, whereby the slowest growing and dominant {001} surface does not have any of the strong coulombic synthons broken at the surface. In contrast, the faster growing {010} and {100} surfaces were predicted to have many more of the strong synthons broken at the surface. The poor adhesivity of the large {001} surface might be consistent with the salmeterol xinafoate based products being formulated with micronised API powders due to the crystal fracture revealing new habits with a high potential for surface binding related to the lower degree of saturated synthons. This suggests that the type of analysis presented here might have more general applications in the formulation design of other API's, to mitigate cases where the as-grown crystals show poor adhesion behaviour with excipients.

## Acknowledgements

One of us (A.M) gratefully thanks EPSRC and Pfizer, for supporting a PhD Scholarship through the Centre for Doctoral Training in Complex Particulate Products and Processes (CP<sup>3</sup>) programme. Many thanks to Darragh Murnane, Simon Connell and CaiYun Ma for their helpful discussion.

## References

- (1) Kaduk, J. A.; Zhong, K.; Gindhart, A. M.; Blanton, T. N. *Powder Diffraction* **2015**, *30*, 333.
- (2) Beach, S.; Latham, D.; Sidgwick, C.; Hanna, M.; York, P. *Organic Process Research and Development* **1999**, *3*, 370.
- (3) Reynolds, D. P. B., P. W. *Glaxo-Wellcome internal report*.
- (4) Murnane, D.; Marriott, C.; Martin, G. P. *International journal of pharmaceuticals* **2008**, *361*, 141.
- (5) Tong, H. H. Y.; Shekunov, B. Y.; York, P.; Chow, A. H. L. *Pharmaceutical Research* **2001**, *18*, 852.
- (6) Tong, H. H.; Shekunov, B. Y.; Chan, J. P.; Mok, C. K.; Hung, H. C.; Chow, A. H. *International journal of pharmaceuticals* **2005**, *295*, 191.
- (7) Tong, H. H. Y.; Shekunov, B. Y.; York, P.; Chow, A. H. L. *Pharmaceutical Research* **2002**, *19*, 640.
- (8) Tong, H. H. Y.; Shekunov, B. Y.; York, P.; Chow, A. H. L. *Journal of Pharmaceutical Sciences* **2008**, *97*, 1025.
- (9) Murnane, D.; Marriott, C.; Martin, G. P. *European journal of pharmaceuticals and biopharmaceutics : official journal of Arbeitsgemeinschaft fur Pharmazeutische Verfahrenstechnik e.V* **2008**, *69*, 94.

- (10) Murnane, D.; Martin, G. P.; Marriott, C. *J Pharm Sci* **2009**, *98*, 503.
- (11) Ramachandran, V.; Murnane, D.; Hammond, R. B.; Pickering, J.; Roberts, K. J.; Soufian, M.; Forbes, B.; Jaffari, S.; Martin, G. P.; Collins, E.; Pencheva, K. *Molecular Pharmaceutics* **2014**, *12*, 18.
- (12) Murnane, D.; Ramachandran, V.; Hammond, R. B.; Pickering, J.; Roberts, K. J.; Soufian, M.; Forbes, B.; Jaffari, S.; Martin, G. P.; Collins, E.; Pencheva, K. In *Respiratory Drug Delivery* 2016; Vol. 1, p 79.
- (13) Hartman, P.; Perdok, W. G. *Acta Crystallogr* **1955**, *8*, 49.
- (14) Dowty, E. *Am. mineral* **1980**, *65*, 465.
- (15) Hartman, P.; Bennema, P. *J Cryst Growth* **1980**, *49*, 145.
- (16) Berkovitch-Yellin, Z. *Journal of the American Chemical Society* **1985**, *107*, 8239.
- (17) Docherty, R.; Roberts, K. J. *J Cryst Growth* **1988**, *88*, 159.
- (18) Docherty, R.; Clydesdale, G.; Roberts, K. J.; Bennema, P. *J. Phys. D-Appl. Phys.* **1991**, *24*, 89.
- (19) A. Gavezzotti, G. C., K.J Roberts and E.M Walker *Theoretical Aspects and Computer Modelling (Chapter 7- The Crystal Habit of Molecular Materials: A Structural Perspective)*, 1997.
- (20) Clydesdale, G.; Roberts, K. J.; Telfer, G. B.; Saunders, V. R.; Pugh, D.; Jackson, R. A.; Meenan, P. *The Journal of Physical Chemistry B* **1998**, *102*, 7044.
- (21) Rosbottom, I.; Roberts, K. J.; Docherty, R. *CrystEngComm* **2015**, *17*, 5768.
- (22) Nguyen, T. T. H.; Rosbottom, I.; Hammond, R. B.; Roberts, K. J.; Marziano, I. *Cryst Grow Des (Submitted)* **2016**.
- (23) Roberts, K. J.; Hammond, R. B.; Ramachandran, V.; Docherty, R. In *Computational Approaches in Pharmaceutical Solid State Chemistry* Abramov, Y., Ed.; Wiley: 2016.
- (24) Pilcer, G.; Amighi, K. *International journal of pharmaceutics* **2010**, *392*, 1.
- (25) Telko, M. J.; Hickey, A. J. *Respiratory Care* **2005**, *50*, 1209.
- (26) Adi, S.; Adi, H.; Chan, H. K.; Finlay, W. H.; Tong, Z. B.; Yang, R. Y.; Yu, A. B. *Journal of Aerosol Science* **2011**, *42*, 285.
- (27) Murnane, D.; Martin, G. P.; Marriott, C. *Pharmaceutical Research* **2008**, *25*, 2283.
- (28) Shur, J.; Price, R. *Advanced Drug Delivery Reviews* **2012**, *64*, 369.
- (29) Jaffari, S.; Forbes, B.; Collins, E.; Khoo, J.; Martin, G. P.; Murnane, D. *Pharmaceutical Research* **2014**, *31*, 3251.
- (30) Ramachandran, V.; Murnane, D.; Hammond, R. B.; Pickering, J.; Roberts, K. J.; Soufian, M.; Forbes, B.; Jaffari, S.; Martin, G. P.; Collins, E.; Pencheva, K. *Molecular Pharmaceutics* **2014**, *12*, 18.
- (31) Cosier, J.; Glazer, A. M. *Journal of Applied Crystallography* **1986**, *19*, 105.
- (32) Diffraction, R. O.; Rigaku Oxford Diffraction: England, 2015.
- (33) Clark, R. C.; Reid, J. S. *Acta Crystallographica Section A Foundations of Crystallography* **1995**, *51*, 887.
- (34) Sheldrick, G. M. *A short history of SHELX* **2008**, *64*, 112.
- (35) Sheldrick, G. M. *Acta Crystallographica Section C: Structural ...* **2015**.

- (36) Dolomanov, O. V.; Bourhis, L. J.; Gildea, R. J.; Howard, J. A. K.; Puschmann, H. *Journal of Applied Crystallography* **2009**, *42*, 339.
- (37) Bruno, I. J.; Cole, J. C.; Edgington, P. R.; Kessler, M.; Macrae, C. F.; McCabe, P.; Pearson, J.; Taylor, R. *Acta Crystallogr B* **2002**, *58*, 389.
- (38) Clydesdale, G.; Roberts, K. J.; Docherty, R. *Journal of Crystal Growth* **1996**, *166*, 78.
- (39) Inc, A. S.; Accelrys Software Inc: San Diego:Accelrys Software Inc., 2013.
- (40) Mayo, S. L.; Olafson, B. D.; Goddard Iii, W. A. *Journal of Physical Chemistry* **1990**, *94*, 8897.
- (41) Gasteiger, J.; Marsili, M. *Tetrahedron Letters* **1978**, *19*, 3181.
- (42) Momany, F. A.; McGuire, R. F.; Burgess, A. W.; Scheraga, H. A. *Journal of Physical Chemistry* **1975**, *79*, 2361.
- (43) Krishnan, K. S.; Roy, S. K. *Physical Review* **1952**, *87*, 581.
- (44) Wulff, G. *Zeitschrift fur Kristallographie und Mineralogie* **1901**, *34*, 449.
- (45) Human, H. J.; Van Der Eerden, J. P.; Jetten, L. A. M. J.; Odekerken, J. G. M. *Journal of Crystal Growth* **1981**, *51*, 589.
- (46) Jetten, L. A. M. J.; Human, H. J.; Bennema, P.; Van Der Eerden, J. P. *Journal of Crystal Growth* **1984**, *68*, 503.
- (47) Thorn, A.; Dittrich, B.; Sheldrick, G. M. *Acta Crystallographica Section A* **2012**, *68*, 448.
- (48) Clydesdale, G.; Docherty, R.; Roberts, K. J. *Computer Physics Communications* **1991**, *64*, 311.
- (49) McArdle, P.; Hu, Y.; Lyons, A.; Dark, R. *CrystEngComm* **2010**, *12*, 3119.
- (50) Walshe, N.; Crushell, M.; Karpinska, J.; Erxleben, A.; McArdle, P. *Crystal Grow Des* **2015**, *15*, 3235.
- (51) Etter, M. C. *Accounts of Chemical Research* **1990**, *23*, 120.
- (52) Etter, M. C.; Macdonald, J. C.; Bernstein, J. *Acta Crystallographica Section B-Structural Science* **1990**, *46*, 256.
- (53) Ålander, E. M.; Rasmuson, Å. C. *AIChE Journal* **2007**, *53*, 2590.
- (54) Ålander, E. M.; Uusi-Penttilä, M. S.; Rasmuson, Å. C. *Powder Technology* **2003**, *130*, 298.
- (55) Uusi-Penttilä, M. S.; Rasmuson, Å. C. *Chemical Engineering Research and Design* **2003**, *81*, 489.
- (56) Chamarthy, S. P.; Pinal, R. *Colloids and Surfaces A: Physicochemical and Engineering Aspects* **2008**, *331*, 68.
- (57) Hooton, J. C.; Jones, M. D.; Harris, H.; Shur, J.; Price, R. *Drug Development and Industrial Pharmacy* **2008**, *34*, 974.
- (58) Murnane, D.; Marriott, C.; Martin, G. P. *Crystal Growth & Design* **2008**, *8*, 2753.
- (59) Murnane, D.; Martin, G. P.; Marriott, C. *Journal of Pharmaceutical Sciences* **2009**, *98*, 503.
- (60) Merrified, D.; Ghadiri, M.; Roberts, K. J. *Journal of Pharmaceutical Sciences (Under Review)* **2016**.

Table 1: Crystallographic Data for Salmeterol Xinafoate from single crystal X-ray diffraction.

<b>Empirical formula</b>	C <sub>36</sub> H <sub>45</sub> NO <sub>7</sub>
<b>Formula weight</b>	603.73
<b>Temperature/K</b>	120.0(2)
<b>Crystal system</b>	triclinic
<b>Space group</b>	P $\bar{1}$
<b>a/Å</b>	9.3848(4)
<b>b/Å</b>	16.1229(6)
<b>c/Å</b>	21.2091(10)
<b><math>\alpha</math>/°</b>	90.156(4)
<b><math>\beta</math>/°</b>	97.687(4)
<b><math>\gamma</math>/°</b>	93.561(4)
<b>Volume/Å<sup>3</sup></b>	3174.0(2)
<b>Z</b>	4
<b><math>\rho_{\text{calc}}</math>/cm<sup>3</sup></b>	1.263
<b>Crystal size/mm<sup>3</sup></b>	0.37 × 0.13 × 0.04
<b>Radiation</b>	MoK $\alpha$ ( $\lambda$ = 0.71073)
<b>2<math>\theta</math> range for data collection/°</b>	6.234 to 62.584
<b>Reflections collected</b>	48367
<b>Goodness-of-fit on F<sup>2</sup></b>	1.053
<b>Final R indexes [I &gt;= 2<math>\sigma</math> (I)]</b>	R <sub>1</sub> = 0.0750, wR <sub>2</sub> = 0.1351

Table 2: Unit cell parameters comparing the previously published structure and newly proposed structure.

Parameters	Previously published structure <sup>1</sup>	This Work
<b>a</b> (Å)	9.1738(9)	9.3848(4)
<b>b</b> (Å)	9.4837(9)	16.1229(6)
<b>c</b> (Å)	21.366(6)	21.2091(1)
<b><math>\alpha</math></b> (°)	82.264(6)	90.156(4)
<b><math>\beta</math></b> (°)	85.253(1)	97.687(4)
<b><math>\gamma</math></b> (°)	62.156(5)	93.561(4)
<b>Volume</b> (Å <sup>3</sup> )	1628.3(6)	3174.0(2)
<b>Z</b>	4	2
<b>Z'</b>	2	4

Table 3a: Strength of top 12 most attractive (top, with subscripted a and illustrated in Figure 8) and 6 most repulsive synthons (bottom, with subscripted r and illustrated in figure 9) along with the molecules involved within the synthons. Distances quoted are the distances between the two centres of gravity of the ions.

A:

Synthon	Molecules Involved	Inter Ion Distance (Å)	Coulombic Contribution (kcal/mol)	Total Interaction (kcal/mol)
A <sub>a</sub>	SA2/XI2	5.43	-27.94	-30.15
B <sub>a</sub>	SA1/XI1	5.58	-27.28	-29.94
C <sub>a</sub>	SA1/XI1	9.64	-18.72	-21.36
D <sub>a</sub>	SA2/XI2	10.10	-18.19	-20.90
E <sub>a</sub>	SA2/XI2	5.24	-12.17	-15.29
F <sub>a</sub>	SA1/XI1	5.64	-11.84	-14.99
G <sub>a</sub>	SA2/XI1	8.23	-8.60	-12.04
H <sub>a</sub>	SA1/XI2	8.98	-8.61	-11.42
I <sub>a</sub>	SA1/XI2	8.18	-10.52	-10.75
J <sub>a</sub>	SA2/XI1	16.71	-9.26	-10.66
K <sub>a</sub>	SA2/XI1	8.76	-10.34	-10.54
L <sub>a</sub>	SA1/XI1	11.34	-9.69	-9.75

B:

Synthon	Molecules Involved	Inter Ion Distance (Å)	Coulombic Contribution (kcal/mol)	Total Interaction (kcal/mol)
A <sub>r</sub>	XI1/XI1	12.35	14.57	14.52
B <sub>r</sub>	XI2/XI2	12.25	14.55	14.50
C <sub>r</sub>	XI1/XI2	8.80	9.29	9.18
D <sub>r</sub>	XI1/XI2	9.35	9.12	9.05
E <sub>r</sub>	XI1/XI2	9.77	9.12	9.02
F <sub>r</sub>	XI2/XI2	9.39	9.02	8.92

Table 4: Slice and attachment energies calculated for the morphologically important surfaces of form I, which were used to construct a prediction of the crystal morphology (Figure 1(b))

<b>Lattice Energy</b>	-67.75
-----------------------	--------

(kcal/mol)			
Surface	Slice Energy (kcal/mol)	Attachment Energy (kcal/mol)	Surface Saturation %
{001}	-63.90	-4.51	94.32
{010}	-43.64	-24.78	64.41
{01-1}	-44.39	-24.03	65.52
{100}	-48.19	-20.23	71.13
{10-1}	-39.13	-29.29	57.76
{1-10}	-38.05	-30.37	56.16
{1-1-1}	-31.92	-36.49	47.11

Table 5: Showing the top three extrinsic synthon contribution from the different major planes, their labels corresponding to the bulk synthons shown in Table 3a. \*Most attractive synthon contributing to the lattice energy was found to be outside the top 12 bulk attractive synthons

Surface	Synthon	Molecules	Distance (Å)	Columbic	Total Interaction
---------	---------	-----------	--------------	----------	-------------------

		<b>Involved</b>		<b>(kcal/mol)</b>	<b>Energy (kcal/mol)</b>
<b>(001)</b>	*	SA2/XI1	13.69	-4.24	-5.32
	*	SA1/XI2	14.26	-4.23	-5.22
	*	SA2/XI2	12.65	-4.95	-4.98
<b>(100)</b>	B <sub>a</sub>	SA1/XI1	5.58	-27.28	-29.94
	E <sub>a</sub>	SA2/XI2	5.24	-12.17	-15.29
	L <sub>a</sub>	SA1/XI1	11.34	-9.69	-9.75
<b>(010)</b>	B <sub>a</sub>	SA1/XI1	5.58	-27.28	-29.94
	F <sub>a</sub>	SA1/XI1	5.64	-11.84	-14.99
	I <sub>a</sub>	SA1/XI2	8.18	-10.52	-10.75



Figure 1(a): SX single crystal with a length of 200 $\mu$ m under dual polarised transmitted mode microscope. Small fractures and debris from other crystals can be observed on the top surface of the crystal.

(b): Attachment energy morphological prediction showing a plate-like morphology with the {001} being the dominant face, along with the smaller {010} and {100} surfaces. The terminating functional groups (surface chemistry) that dominate each of the faces are shown in (c, d, e). These functional groups are enlarged in squares.

Figure 2: DSC thermal profiles. The dashed trace is of the recrystallised material and shows only one major melting event at approximately 125°C and a small bump at approximately 137°C. The solid trace is of the as received micronized material and shows two major melting points and a polymorph transition event.

Figure 3(a): The  $P\bar{1}$  triclinic unit cell of salmeterol xinafoate form I solved by single crystal XRD. The colouring indicates the symmetrically equivalent molecules found in the unit cell. The legend; SA1, SA2, XI1 and XI2 notating the four molecules present in the asymmetric unit; (b) the first pair of salmeterol and xinafoate ions, coloured green and red in the unit cell; (c) the second pair of salmeterol and xinafoate ions, coloured blue and yellow in the unit cell. The disorder positions are shown within the blue circles.

Figure 4: Packing of the salmeterol xinafoate form I structure demonstrating that the strong interactions between the oppositely charged ions and the H-bonds run closest to parallel to the a and b axes, and less along the direction of the a-axis.

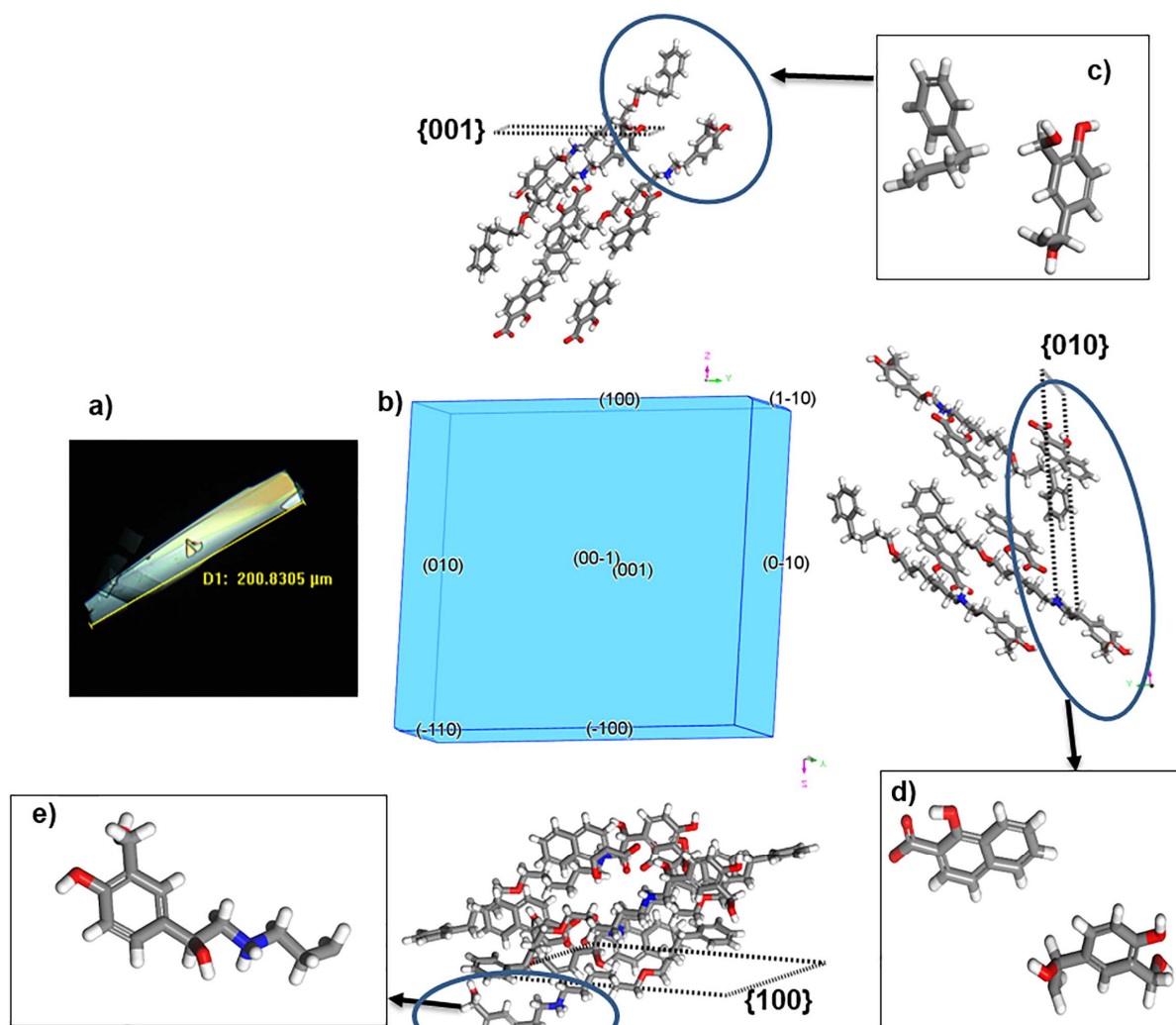
Figure 5(a): Overlays of the two salmeterol conformers (SA1 and SA2). Main difference in conformation is the rotation of the  $(\text{CH}_2)_3(\text{C}_6\text{H}_5)$  groups (circled); (b): Torsional angle at the centre of major rotation between the two salmeterol molecules, along the O4-C16-C17-C18 (-178.986°) and O11-C52A-C53A-C53A-C54A (72.127°), which results in the two separate conformers.

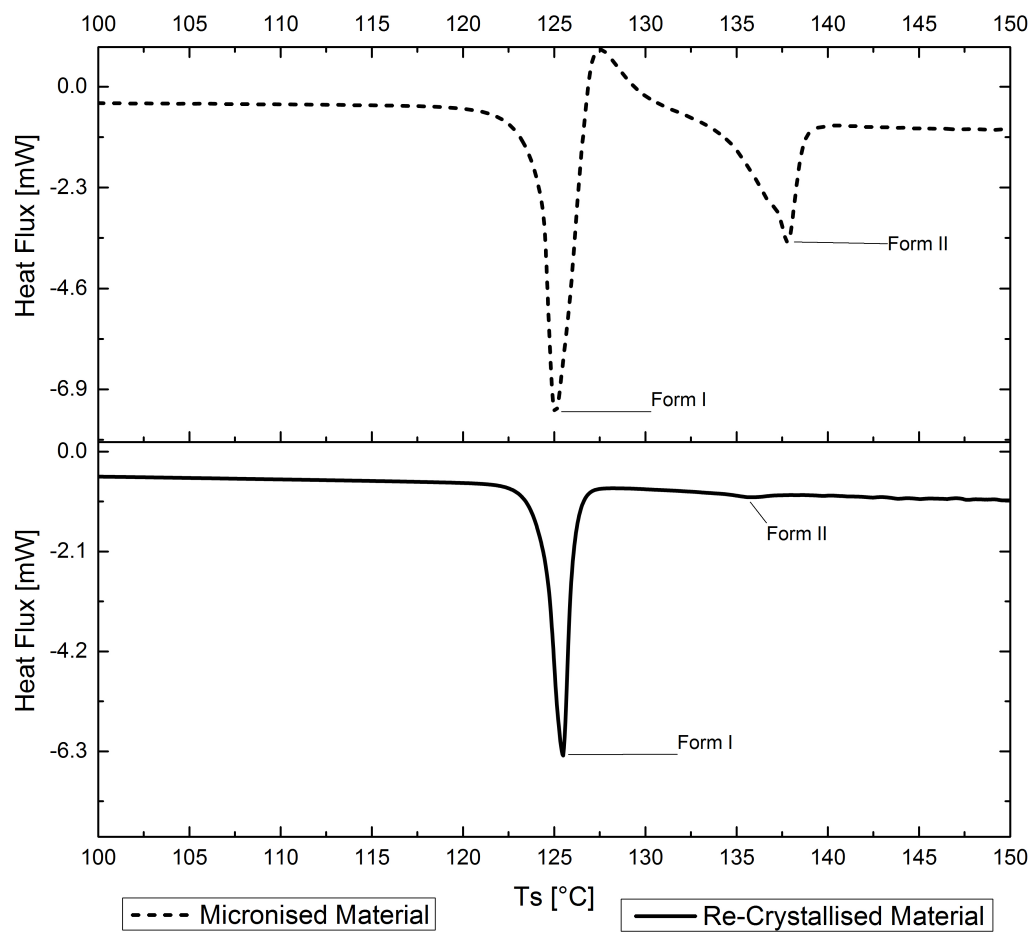
Figure 6: Lattice energy convergence as a function of limiting radius for SXI, indicating that interactions above approximately 30 Å are relatively unimportant to the stabilisation of the lattice.

Figure 7: The % contribution to the lattice energy from the different molecular groups of the asymmetric unit. The percentages are summed from all four molecules of the asymmetric unit and collapsed onto the molecular structure of the two molecules for simplicity. The contributions of the salt pairs were found to be broadly similar and were therefore averaged.

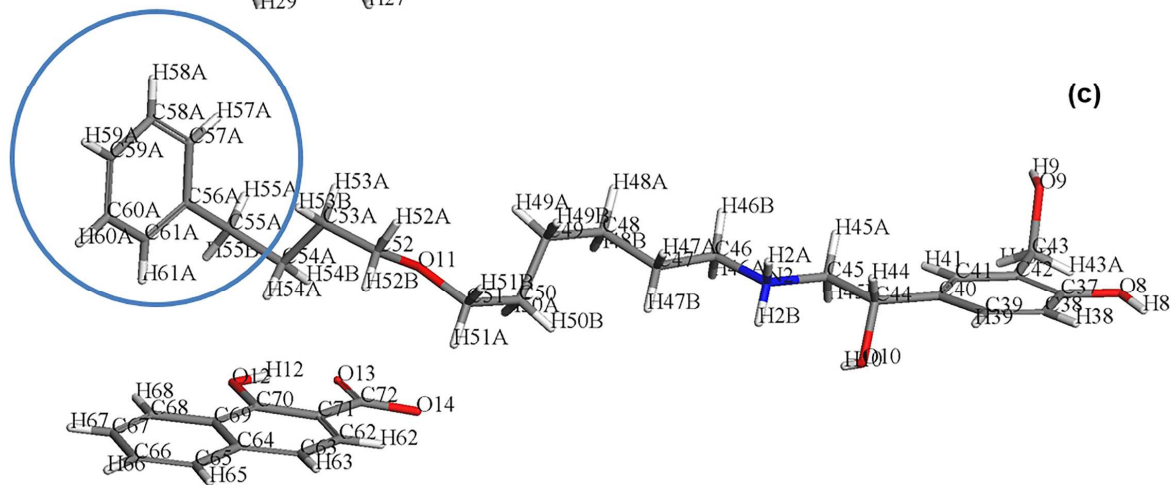
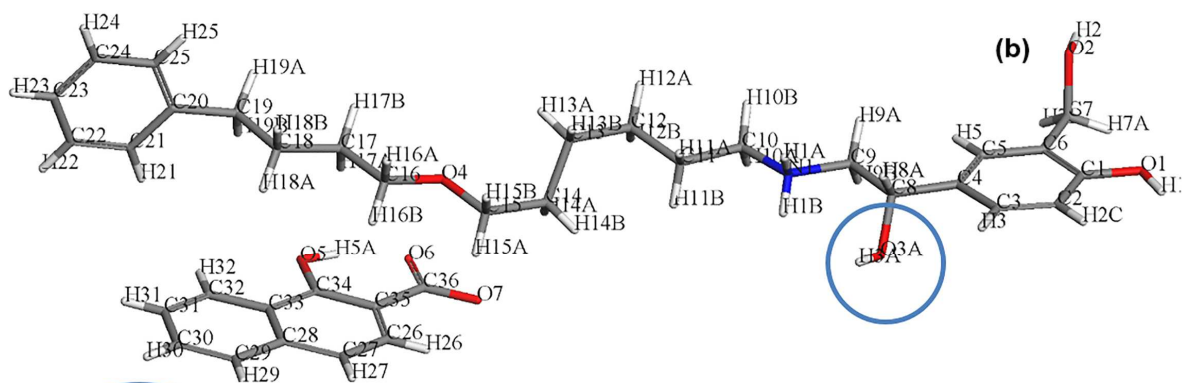
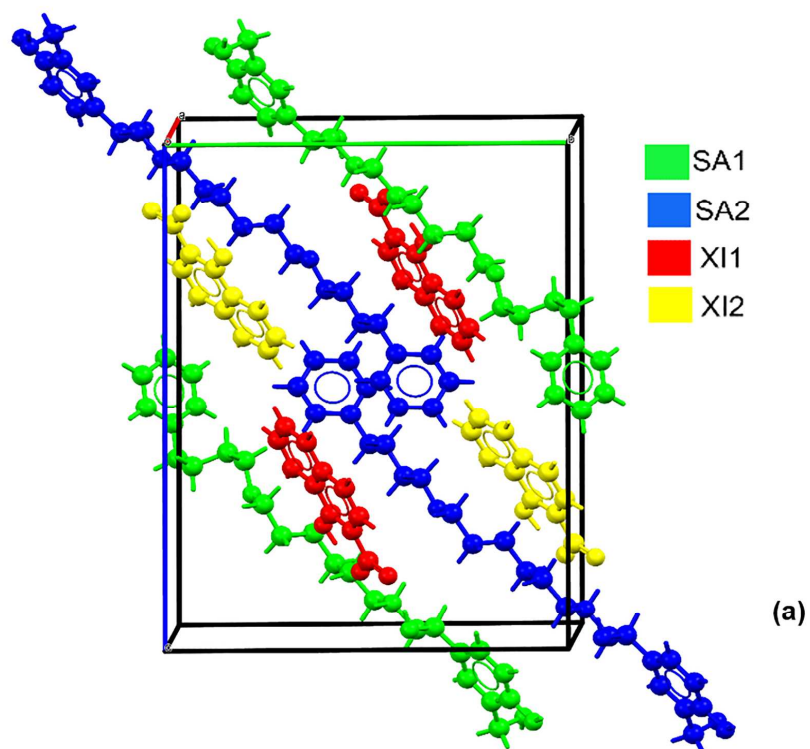
Figure 8: Molecular orientation of the top 12 attractive synthons shown in Table 2a, indicating that the major interactions were between the oppositely charged ions. Similar interaction types that are only different since they are between the different salt pairs are shown only once and labelled as two synthons. H-bonding synthons enlarged for clarity of H-bonding atoms. All distances are quoted between  $\text{COO}^- \cdots \text{NH}_2^+$ .

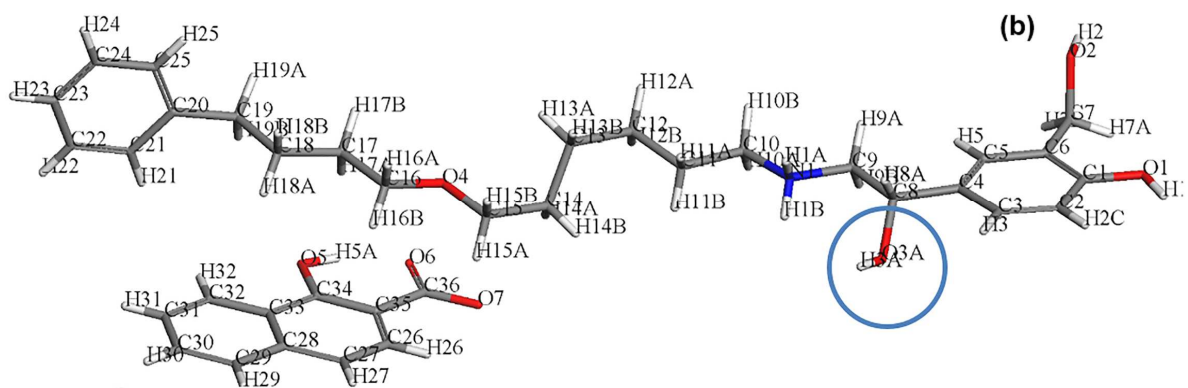
Figure 9: Molecular orientation of the top 4 repulsive synthons shown in Table 3b, indicating that the major repulsions were between the xinafoate ions. All distances are quoted between C-C atoms.

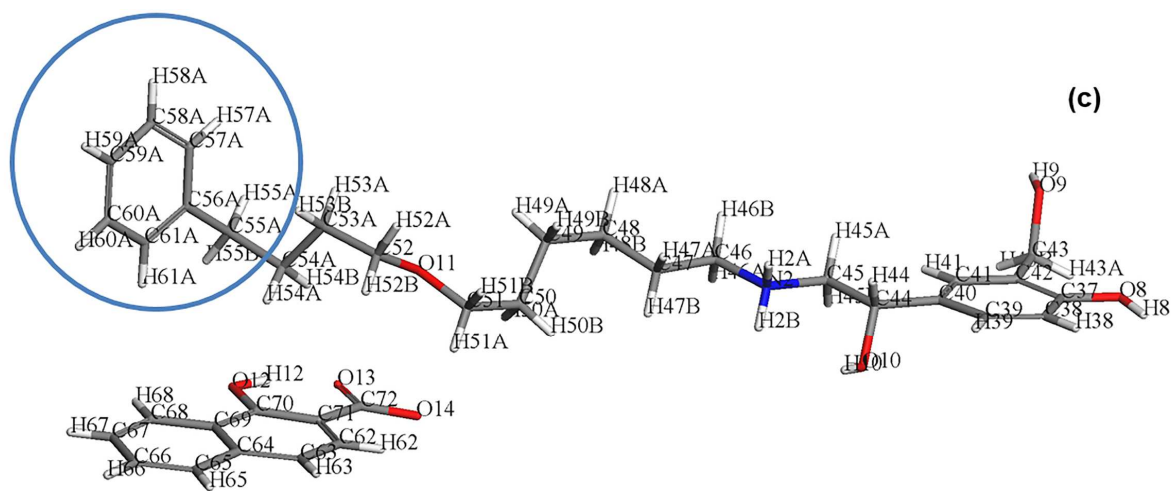


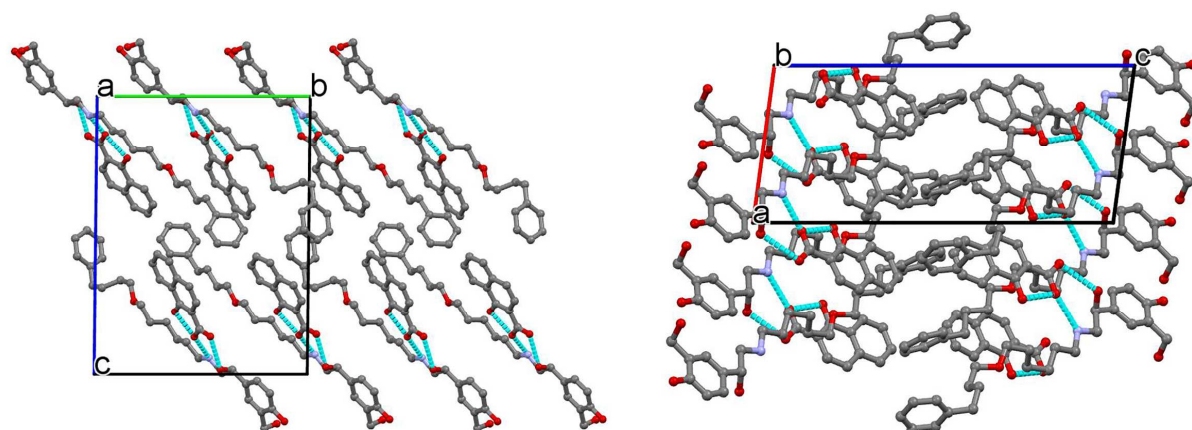


ACCEPTED

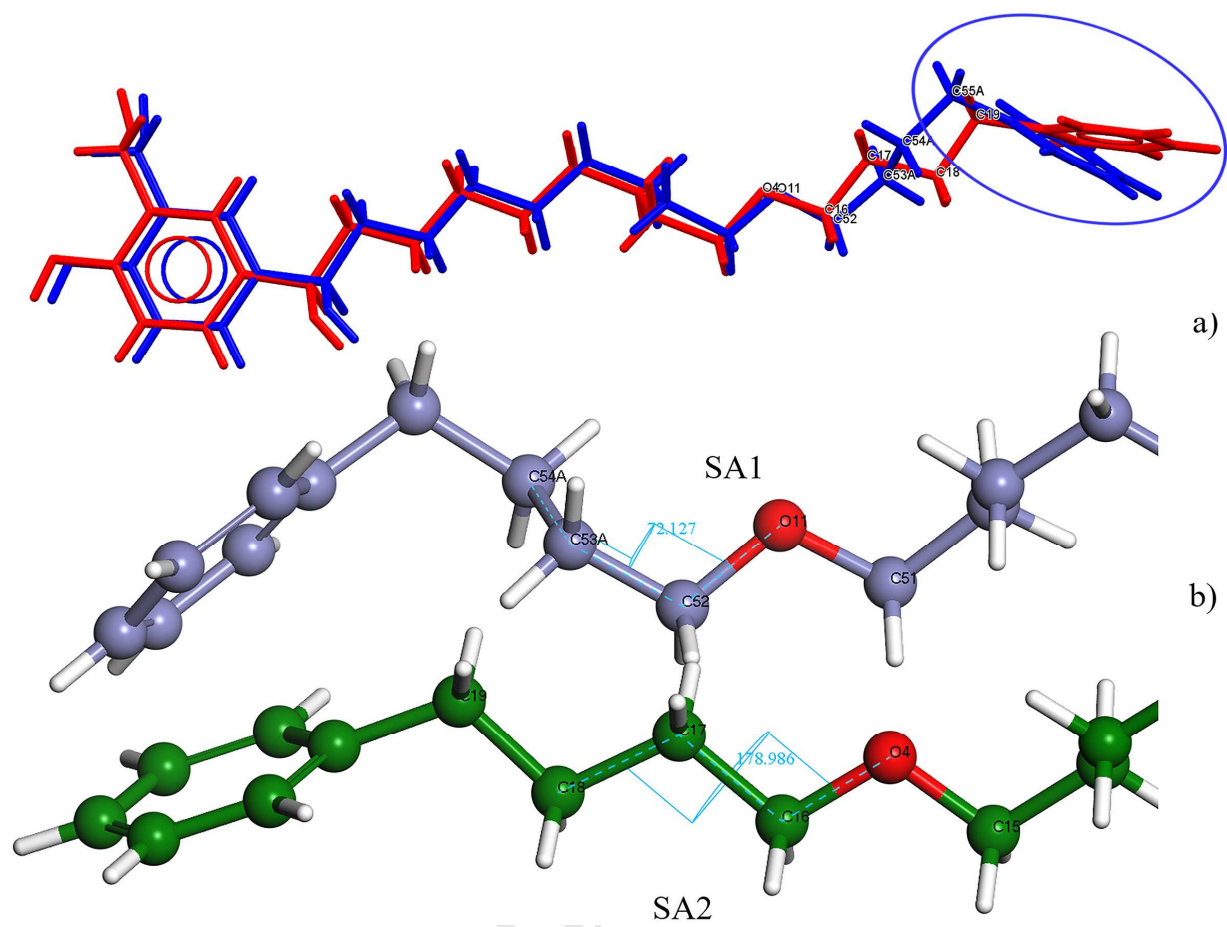




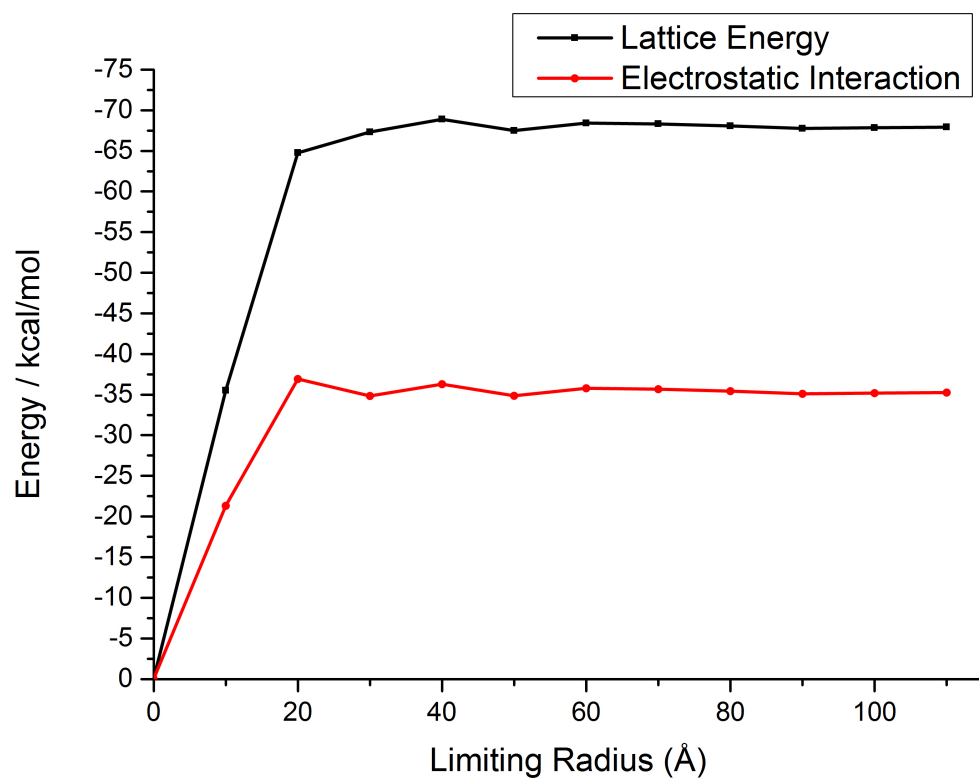


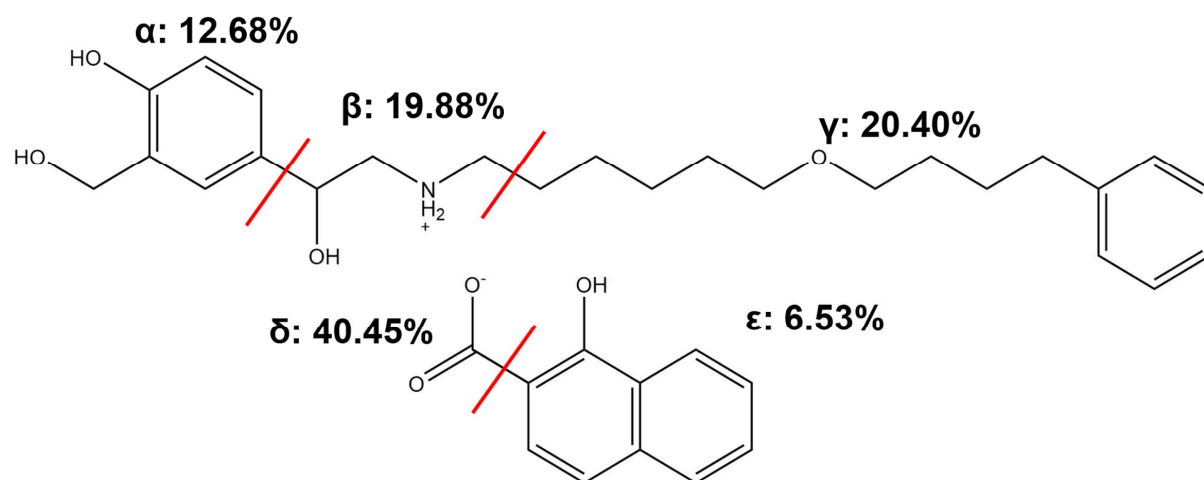


ACCEPTED MANUSCRIPT

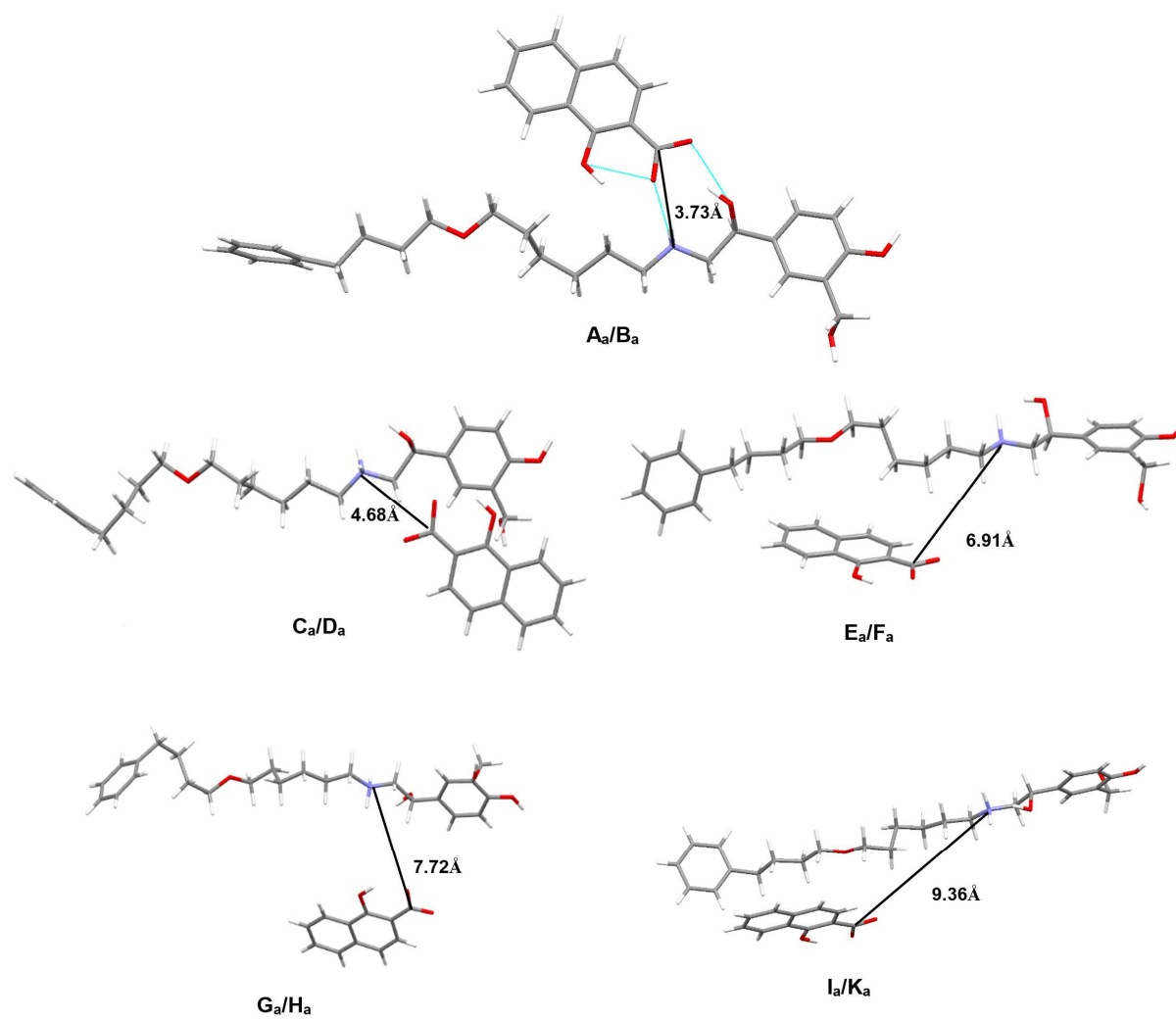




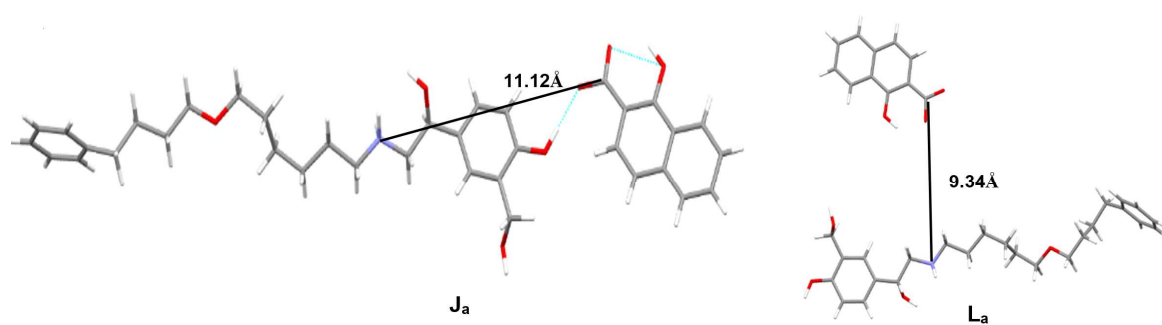


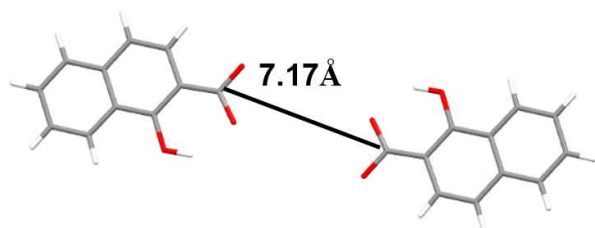
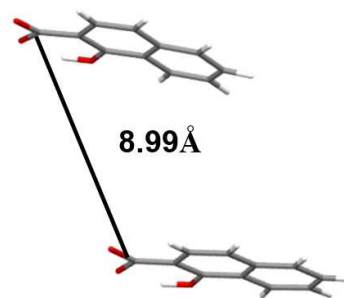
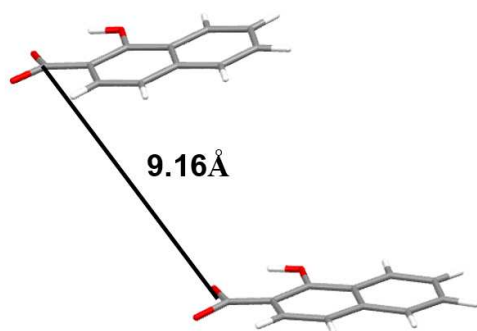
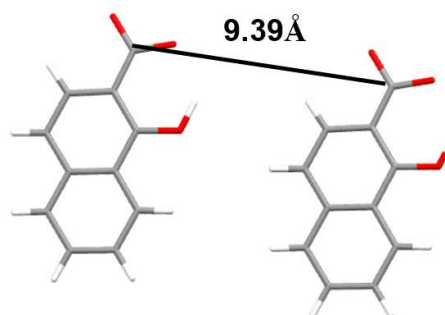


ACCEPTED MANUSCRIPT



ACCEPTED



**Ar****Br****Cr****Dr**

ACCEPTED